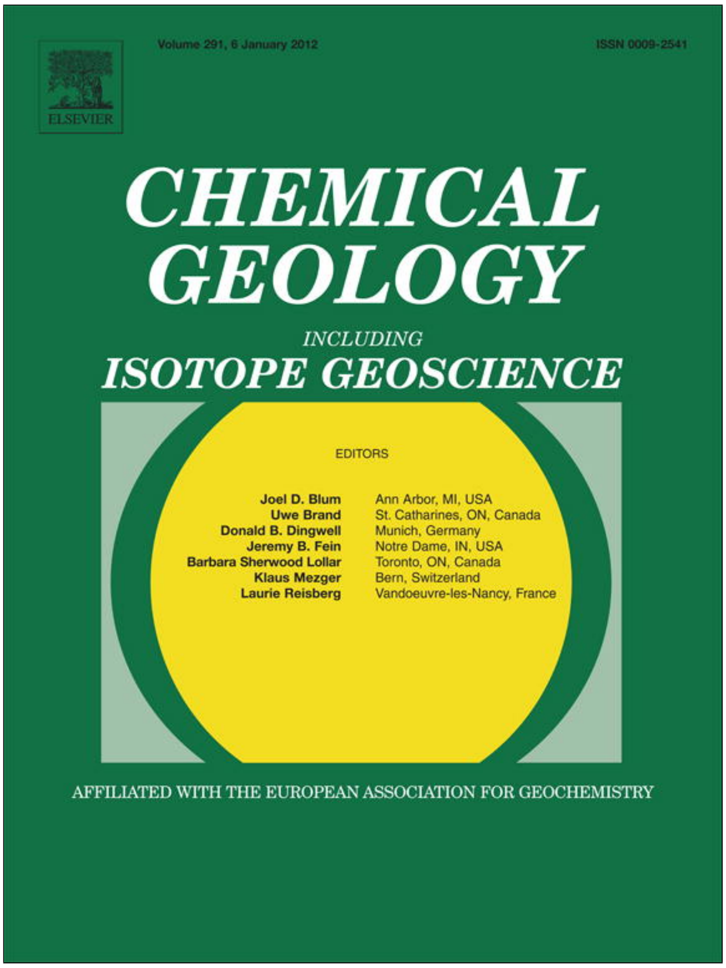

Volume 291, 6 January 2012

ISSN 0009-2541

ELSEVIER

CHEMICAL GEOLOGY

INCLUDING

ISOTOPE GEOSCIENCE

AFFILIATED WITH THE EUROPEAN ASSOCIATION FOR GEOCHEMISTRY

Chemical Geology 300-301 (2012) 14–23

Contents lists available at SciVerse ScienceDirect

Chemical Geology

journal homepage: www.elsevier.com/locate/chemgeo

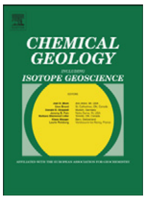

Examining the chemistry and magnetism of magnetotactic bacterium *Candidatus* Magnetovibrio blakemorei strain MV-1 using scanning transmission X-ray microscopy

Samanbir S. Kalirai [a], Karen P. Lam [a], Dennis A. Bazylinski [b], Ulysses Lins [c], Adam P. Hitchcock [a],*

[a] *Department of Chemistry and Chemical Biology, McMaster University, Hamilton, ON, L8S 4M1 Canada*
[b] *School of Life Sciences, University of Nevada at Las Vegas, Las Vegas, NV, 89154-4004, USA*
[c] *Departamento de Microbiologia Geral, Instituto de Microbiologia Professor Paulo de Góes, Universidade Federal do Rio de Janeiro, 21941-590, Rio de Janeiro, RJ, Brazil*

ARTICLE INFO

Article history:
Received 17 October 2011
Received in revised form 11 January 2012
Accepted 12 January 2012
Available online 21 January 2012

Editor: J. Fein

Keywords:
magnetotactic bacteria
magnetosomes
STXM
XMCD
NEXAFS
Fe 2p

ABSTRACT

Scanning transmission X-ray microscopy (STXM) measurements at the C K, O K and Fe L$_3$ edges were used to study the magnetotactic bacterium *Candidatus* Magnetovibrio blakemorei strain MV-1 on an individual cell basis. Improved data acquisition methodologies resulting in higher quality results are presented. Visualization of magnetosomes from their O K-edge signal is demonstrated. The Fe L$_3$ X-ray magnetic circular dichroism (XMCD) signal was used to characterize the magnetic properties of several MV-1 cells on an individual magnetosome basis. The absolute magnetic moment from two cells was evaluated and found to be 0.93(6) of that of saturated abiotic magnetite, or 3.6(2) μB. Previously observed excess Fe (II) was not found in this study, suggesting the prior observation (Lam et al., Chem. Geol 270 (2010) 110) may have been a radiation damage artifact.

1. Introduction

Synchrotron-based soft X-ray STXM (Ade and Hitchcock, 2008; Howells et al., 2007) uses near edge X-ray absorption fine structure (NEXAFS) as the contrast mechanism to provide elemental and chemically sensitive imaging at ~25 nm spatial resolution. NEXAFS spectra (Stöhr, 1991) probe the electronic, magnetic and geometric structure of materials by exciting core electrons into empty valence shells. Analysis of image sequences recorded with STXM yield quantitative maps of inorganic and organic materials with elemental specificity and chemical speciation. Since the C, N, O, K-edge and Fe, S, Ca L-edge core levels are well separated, studies at multiple edges provide the ability to determine spectra and quantitative spatial distributions of major biochemical components (protein, lipids, polysaccharides, etc.) in addition to the magnetite magnetosomes, which are the focus of this study. In this regard, STXM has significant advantages relative to basic microscopic techniques due to its ability to discriminate spectrally, and to provide spectra subjectable to detailed analysis. Further, it offers many advantages over spatially unresolved spectroscopies in the case of environmental and biogeochemical samples, which are usually highly anisotropic. STXMs at beamlines based on elliptically polarizing undulators (EPU) use the capability to vary the orientation of circularly and linearly polarized light to measure and map both linear (Najafi et al., 2008) and magnetic dichroism (Coker et al., in press; Lam et al., 2010). This allows STXM to be used not only as a spatially resolved chemical analysis tool but also as one that discriminates charge and magnetic anisotropies.

X-ray magnetic circular dichroism (XMCD) (Stöhr, 1999; Stöhr and Siegmann, 2006) is a branch of X-ray absorption spectroscopy that provides information about the magnetic structure of materials. The XMCD signal is defined as the difference in edge-jump normalized absorption spectra recorded with parallel and anti-parallel alignment of the photon spin and total magnetic moment vectors ($OD_{\uparrow\uparrow}$–$OD_{\uparrow\downarrow}$) (Stöhr and Siegmann, 2006). Detailed XMCD sum rule-based analysis of XMCD signals can be used to determine the total magnetic moment, as well as the individual contributions from spin versus orbital magnetic moments (Stöhr, 1999; Stöhr and Siegmann, 2006). However, sum rule analyses require very high statistical quality and

---

* Corresponding author. Tel.: +1 905 525 9140.
E-mail address: aph@mcmaster.ca (A.P. Hitchcock).

0009-2541/$ – see front matter © 2012 Elsevier B.V. All rights reserved.
doi:10.1016/j.chemgeo.2012.01.005

extended data ranges (Goering et al., 2006b). They have been applied to the complex XMCD signals of magnetite (Goering et al., 2006a, 2006b, 2007; Huang et al., 2004; Kuiper et al., 1997; Pellegrain et al., 1999; Pérez et al., 2009) and other transition-metal oxides (Goering et al., 2002). It is noteworthy that in many situations (e.g. Fe_2O_3 versus Fe_3O_4, Pérez et al., 2009), the Fe L-edge X-ray absorption spectra can be rather similar, yet have quite distinct XMCD. There are also size dependent changes in XMCD of nanoparticles (Pellegrin et al., 1999).

XMCD of abiotic and biologically produced magnetite has been reported by several groups (Carvallo et al., 2008; Goering et al., 2006a, 2007). Staniland et al. (2007) used XMCD to investigate the kinetics of in-vivo formation of magnetite magnetosomes in Magnetospirillum gryphiswaldense strain MSR-1. Coupling of STXM to XMCD is a logical and desirable approach for studying the magnetic properties of biogenic (and abiogenic) magnetite in cases such as magnetotactic bacteria, where spatial resolution is required to investigate the magnetic properties of individual cells and individual magnetosomes. Recently, we reported the first such measurements (Lam et al., 2010). In this work, we report a significant improvement in our experimental results, and show for the first time measurements of complementary core edges. In addition we have quantitatively evaluated the total magnetic moment for several cells of the *Candidatus* Magnetovibrio blakemorei (MV-1) magnetotactic bacterial cells.

There are three types of Fe sites in the magnetite crystal structure — a tetrahedral site with Fe (III)-d^5 oxidation state and octahedral sites occupied by Fe (II)-d^6 and Fe (III)-d^5. The Fe L_3 ($2p_{3/2}$) XMCD spectrum of magnetite (Goering et al., 2006a, 2007; Kuiper et al., 1997; Pellegrin et al., 1999) shows three characteristic peaks which have been correlated based on atomic multiplet calculations to the three distinct sites: a negative peak at 708.1 eV arising mostly from the d^6 O_h (Fe (II)) site; the positive peak at 709.1 eV associated with the d^5 T_d (Fe (III)) site; and the negative peak at 709.9 eV arising mostly from the d^5 O_h (Fe (III)) (Kuiper et al., 1997; Pattrick et al., 2002). The site-specific character of the XMCD spectrum of magnetite has been used to determine site occupancies, which allow for differentiation between biological and abiotic (mineral) magnetite (Carvallo et al., 2008; Coker et al., 2007). Other computational results (Antonov et al., 2003; Leonov et al., 2004, 2006) indicate that the correlation between the XMCD spectral features and the projected site specific contributions is more convoluted than that proposed by Pattrick et al. (2002). Nolle et al. (2009) have shown that experimental XMCD spectra of complex mixed oxide systems can be deconvoluted to generate species- and site-specific signals and evaluate relative amounts of magnetic and non-magnetic contributions.

Magnetotactic bacteria (MTB) are gram-negative, microaerophilic/anaerobic bacteria found in both freshwater and marine aquatic environments (Bellini, 1963a,b; Bellini, 2009; Blakemore, 1975; Frankel and Blakemore, 1980; Frankel et al., 1979). Blakemore (1975) showed that MTB use a phenomenon known as magnetotaxis in which the MTB use the Earth's magnetic field to orient in order to more efficiently locate and maintain position in anaerobic or microaerobic regions of the sediment (known as the oxic-anoxic transition zone) where the chemical/redox environment is optimal for their metabolism (Bazylinski, 1995; Frankel and Bazylinski, 1994). The magnetotaxis effect is possible due to the mineralization of membrane-bounded, intracellular magnetic nanoparticles, referred to as magnetosomes. Depending on the species, magnetosome crystals are composed of ferrimagnetic magnetite (Fe_3O_4) or greigite (Fe_3S_4) (Heywood et al., 1991) and typically range in size from 35 to 120 nm (Bazylinski and Frankel, 2004). Each crystal is surrounded by a phospholipid bilayer membrane which is 3–4 nm thick (Gorby et al., 1988). Magnetosome crystals are typically in the size range of single magnetic domains, thereby maximizing the magnetic moment of each particle (Frankel and Blakemore, 1980) by avoiding the thermal instability of the superparamagnetic regime (Dunlop, 1973) or reduction in magnetic strength due to domain formation.

Differences in the physical properties of magnetosomal and abiotic magnetite and greigite indicate that biomineralization of magnetosome minerals by MTB is a highly controlled biological process. For example, elongation of magnetosome crystals along the (111) axis and their high chemical purity provide a major distinction between biologically- and abiologically-synthesized magnetite single crystals which has potential relevance to exobiology (Carvallo et al., 2008; Jimenez-Lopez et al., 2010; Thomas-Keprta et al., 2000). Physiological evidence also supports a strongly controlled biomineralization of magnetosome minerals. For example, Komeili et al. (2004) have shown the presence of magnetosome vesicles prior to magnetosome formation. The formation of co-aligned magnetosome chains further suggests biological control of their synthesis.

Because of their narrow size distribution, high chemical purity and magnetic response, magnetosome magnetite has garnered much interest for potential applications in medicine, environmental science and technology. Both magnetotactic bacteria and magnetosomes have been proposed for use in nanorobotic devices for mobilized and targeted drug delivery since they are readily located and manipulated using external or internal magnetic fields (Albrecht et al., 2005; Ceyhan et al., 2006; Martel et al., 2009). Studies of the mechanisms of formation of magnetosomes are motivated by the desire to have an in depth understanding of this fascinating example of biomineralization as well as the potential for enhancing biotechnological and environmental applications.

The magnetic properties of magnetosomes have been characterized with several techniques including magnetic force microscopy (Albrecht et al., 2005), low-temperature SQUID magnetometry (Moskowitz et al., 1993), ferromagnetic resonance (Charilaou et al., 2011; Fischer et al., 2008; Weiss et al., 2004) and coercivity deconvolution (Egli, 2004). Electron holography measurements in transmission electron microscopes (TEM) have been used to visualize the magnetic properties of magnetosomes (Dunin-Borkowski et al., 1998; McCartney et al., 2001; Simpson et al., 2005). Fe L_{23} X-ray magnetic circular dichroism (XMCD) has been used without spatial resolution to study magnetosome extracts (Coker et al., 2007, 2009; Staniland et al., 2007, 2008) and biologically-generated, extracellular magnetic iron oxide deposits (Coker et al., 2006, 2007, 2008, 2009). The first XMCD study of individual magnetosomes within a single MTB cell using synchrotron-based scanning transmission X-ray microscopy (STXM) was reported by our group (Lam et al., 2010). This approach was recently used by Coker et al. (in press) to study extracellular magnetite generated by *Shewanella oneidensis* strain MR-1. Here we report further STXM investigations of *Candidatus* Magnetovibrio blakemorei strain MV-1, using both biologically-sensitive (C 1s, O 1s) and magnetically-sensitive (Fe 2p) edges.

2. Experimental

2.1. Preparation of magnetotactic bacterial cells

Cells of *Candidatus* Magnetovibrio blakemorei were grown in liquid culture as previously described by Dean and Bazylinski (1999). 5–10 μL of a concentrated liquid culture was placed onto a 200-mesh glow-discharged copper grid coated with polyvinyl formal (formvar). The droplet was left standing for several minutes before the liquid was wicked away with filter paper. The grids were left to dry in air.

2.2. STXM-XMCD measurements

Details of the Canadian Light Source (CLS) 10ID-1 soft X-ray spectromicroscopy beamline (Kaznatcheev et al., 2007), the STXM (Kilcoyne et al., 2003), and the measurement procedures (Ade and Hitchcock, 2008; Lam et al., 2010) have been presented elsewhere. Briefly, monochromatic X-rays are focused by a zone-plate (a circular diffraction grating) to a small spot (31 nm, based on the Raleigh criterion, and assuming fully coherent illumination). The sample is mounted on a piezo stage and its position relative to the focussed X-ray spot is controlled at the 2–3 nm level by laser interferometry. The sample is raster scanned while detecting the transmitted flux to form an image. Signals through sample regions (I) are normalized to signals from off-sample regions (I_o) to derive the optical density, $OD = -\ln(I/I_0)$. Acquisition of a sequence of images at energies through an X-ray absorption edge provides spatially resolved NEXAFS spectra.

It is possible in general to measure XMCD either by varying an applied magnetic field, or by comparing the signals recorded with left and right circular polarized X-rays. Since our goal is to interrogate the intrinsic magnetic properties of the magnetotactic bacteria with minimal modifications to their natural state, we have used alternation of the photon polarization. In order to do so it is essential to correctly position the sample relative to the X-ray beam, since XMCD signals only arise from that part of the magnetization for which the sample magnetism is coaxial with the X-ray propagation axis (Stöhr and Siegmann, 2006). The magnetism of a chain of magnetosomes is generally along the long axis of the cell, and thus in the plane of the grid or Si_3N_4 window supporting the cells. In order to generate a non-zero projection of the magnetization vector onto the X-ray propagation axis, the sample is mounted at a 30° angle. For this purpose a sample holder with a wedge was used to create a fixed 30° tilt along the horizontal axis between the surface normal and incoming X-rays. Alternatively, the sample is mounted on a tomography holder (Johansson et al., 2007), which allows arbitrary polar rotation. For XMCD studies, a 30° rotation angle is used. In either of these rotated geometries, horizontal or near-horizontally-oriented magnetosome chains give the largest XMCD signal; vertically oriented chains have zero XMCD. For a perfectly horizontal magnetosome chain, 50% of the magnetization vector is projected on the X-ray propagation axis. Deviation from horizontal further attenuates the XMCD signal by the cosine of the deviation angle.

Improvements to the Elliptically Polarizing Undulator (EPU) at the CLS soft X-ray spectromicroscopy beamline and the STXM_control software have resulted in more reliable data collection relative to our earlier work (Lam et al., 2010). The rate at which the EPU can switched from left circularly polarized (LCP) to right circularly polarized (RCP) light, while having the electron beam orbit stabilized, was significantly improved such that switching between right and left circular polarization can now be done in ~8 s. This allows for alternating RCP/LCP measurements at each photon energy (concurrent mode, method B) which significantly improves reliability over the original procedure used by Lam et al. (2010) in which complete image sequences were measured with one circular polarization, before changing to the opposite polarization (successive mode, method A). In method A each image sequence took ~5 h to collect, a period over which there is significant drift in the instrumental response, which resulted in data which required extensive and careful correction. In the improved procedure the circular polarization is alternated at each photon energy (RCP/LCP) (concurrent mode, method B). This results in substantially more precise data, which greatly reduces the effort needed to extract the XMCD. For example, the image alignment parameters for the RCP and LCP polarization subsets are the same since the images for the two polarizations at each photon energy take only a few minutes to collect. A further significant improvement was made by using the point-by-point rather than the line-at-a-time acquisition mode, which required improvements to the STXM_control software. The point-by-point mode significantly improves spatial precision and thus the quality of the individual images and the precision of the spectra extracted from small regions such as individual magnetosomes. The effects of both improvements on data quality are documented below.

2.3. XMCD data analysis

In this work, X-ray absorption spectra are plotted on the as-recorded optical density scales. As the optical density of individual magnetosomes is very weak, there is no absorption saturation, however, the low OD makes the experiment quite challenging. In order to evaluate the total magnetic moment, we have compared quantitatively the strength of the MV-1 XMCD signal to that of abiotic magnetite, since the latter possesses a saturated magnetic moment and has been carefully measured in a strong magnetic field (Goering et al., 2006a). To perform the quantitative comparison, the Fe L_3 spectra of MV-1 recorded with left (LCP) and right (RCP) polarized light are first carefully background-subtracted using identical background functions (typically linear, which is valid over the short energy span of the L_3 signal), before the intensities of the Fe L_3 component are scaled (again using the same factor for both LCP and RCP) to make a best match to the L_3 spectrum of abiotic magnetite (Goering et al., 2006a) outside of the L_3 peak (between 702–705 eV, and 714–718 eV) prior to subtraction. In this way, the ratio of the integrated XMCD signal (705–715 eV) from an MV-1 sample to that for abiotic magnetite provides a quantitative measure of the magnitude of the XMCD and thus the total magnetic moment for that MV-1 sample. In this work we chose to measure only the L_3 component since our L_3 measurements at present have higher statistical accuracy compared to those at the L_2 component. Also, analysis of the L_2 XMCD requires correction for overlap with the magnetically-sensitive L_3 extended fine structure signal (Goering et al., 2006a, 2006b). This requires very long range spectra, which are prohibitively time consuming when making spectroscopic measurements using the image sequence approach. Since only L_3 data has been measured, it is not possible to make a sum rule analysis but the total moment was evaluated by quantitative comparison to the XMCD of abiotic magnetite.

3. Results

3.1. Documenting improved performance

Fig. 1a indicates how the polarization changes with time in the successive (Method A), versus the concurrent (Method B) modes. The benefits of changing to the concurrent mode are documented in Figs. 1–3. An example of the improved STXM-XMCD quality is presented in Fig. 1, which compares the Fe L_3 NEXAFS and XMCD spectra of a magnetosome chain within one MV-1 cell, recorded with method A (July 2009, Fig. 1b) and with method B (September 2009, Fig. 1c). Fig. 1d is a comparison of the fractional noise level in the two measurements, obtained by subtracting an appropriately scaled version of the Fe L_3 XMCD of synthetic magnetite reported by Goering et al. (2007) from the measured XMCD of the magnetosome chain. Clearly the noise level is much larger in the method A measurements (refer to blue line in Fig. 1d) even though the dimensions of the chains and the experimental conditions were similar for the two measurements. The lengths of the magnetosome chains in Figs. 1b (8 magnetosomes) and 1c (9 magnetosomes) are 0.54 μm and 0.63 μm, respectively. The pixel dwell times for the two data sets were 5 and 6 ms, respectively. The exit slits were 8 or 10 μm, with the value chosen so that the detected signal of the incident beam off the magnetosome chain was below 20 MHz in order to ensure a linear detector response. The noticeable improvement in spectral quality and reproducibility with method B (alternating polarization at each photon energy) can be attributed to the fact that the incident beam intensity at CLS is more stable over shorter than longer periods. In addition to plotting the spectra for each polarization, Figs. 1b and 1c also plot the XMCD spectra obtained by subtracting the anti-parallel (red) spectrum from the parallel spectrum (green). The XMCD spectra of the magnetosome chains are compared to that of the XMCD spectrum of mineral magnetite (Goering et al., 2007), multiplied by a factor of

0.5 to account for the projection of the in-plane magnetization of the magnetosome chain onto the X-ray propagation direction (a 30° tilt angle was used).

In Fig. 1b, the spectra were measured successively for each polarization (method A); thus beam fluctuations and intensity normalized stacks are affected by drifts in the storage ring and beamline conditions. This yields poorer statistics and a poorer match of the pre-edge absorption profiles of the parallel and anti-parallel spectra. However, when the spectra are recorded concurrently by alternating the polarization at each successive energy (method B), the result is less dependent on the long-term stability of the storage ring and beamline. For samples with relatively long exposures times, as is the case in STXM-XMCD measurements, irradiation causes a build-up of carbon on the sample due to cracking of surface-adsorbed hydrocarbons. Although this was a major concern for measurements using method A, the effect is negligible for measurements using method B since the slow build-up of carbon is tracked in the off-cell portion which is the source of the I_o signal used for conversion from transmission to optical density. This can be seen by comparing Fig. 2 (method A, successive polarization measurements) and Fig. 3 (method B, concurrent polarization measurements). These figures contrast the difference in the average of all images acquired with (i) left circular polarization (Figs. 2a, 3a) and (ii) right circular polarization (Figs. 2b, 3b), as well as the difference in the LCP and RCP signals in the (iii) pre-edge (704–706 eV, Figs. 2c, 3c) and (iv) iron L_3 (708–711 eV, Figs. 2d, 3d) regions. With the successive measurement mode (method A), the OD range is 0.08 for the pre-edge difference image and 0.09 for the Fe L_3 difference image. This is a significant portion of the total OD in the Fe L_3 peak (0.2–0.3). Spectral distortions are more pronounced in the cellular biomolecular region (used for the I_0) than the magnetosome region, as biological material is more susceptible to radiation damage (Toner et al., 2005). The pre-edge difference image for method A (Fig. 2c) shows a radiation-damage-related OD difference pattern that is systematic and consistent with the structure. In contrast, for method B, the pre-edge difference image (Fig. 3c) is uniform and un-structured, and the total OD range is only 0.02. By switching to concurrent polarization measurements (method B), the decreased data collection time has improved the overall statistical quality while lowering radiation-damage-induced artifacts. The close correlation between the biogenic XMCD and the scaled reference spectrum of magnetite (Goering et al., 2007) (Fig. 1c) exemplifies the increased reliability of concurrent polarization measurement mode.

Fig. 4 documents the improvements that result from acquiring images in the point-by-point mode rather than line-at-a-time mode, in both method A and method B. The absolute OD differences between line-at-a-time and point-by-point mode show that the point-by-point mode is superior (as indicated by less jitter at the edges of the magnetosomes), largely due to the higher spatial precision provided by the point-by-point mode. The absolute OD differences (Fig. 4c and d) are lower and there is a smoother variation in the signal when point-by-point mode is used in conjunction with method B.

3.2. Fe L_3 XMCD studies of cells of strain MV-1

Fig. 5a shows a STXM image at 709.8 eV of an array of strain MV-1 cells. The curved-rod shape of the cells is characteristic of the MV-1 marine vibroid species. Fig. 5b shows a false color image of the upper right area of Fig. 5a in which the iron signal (the difference of

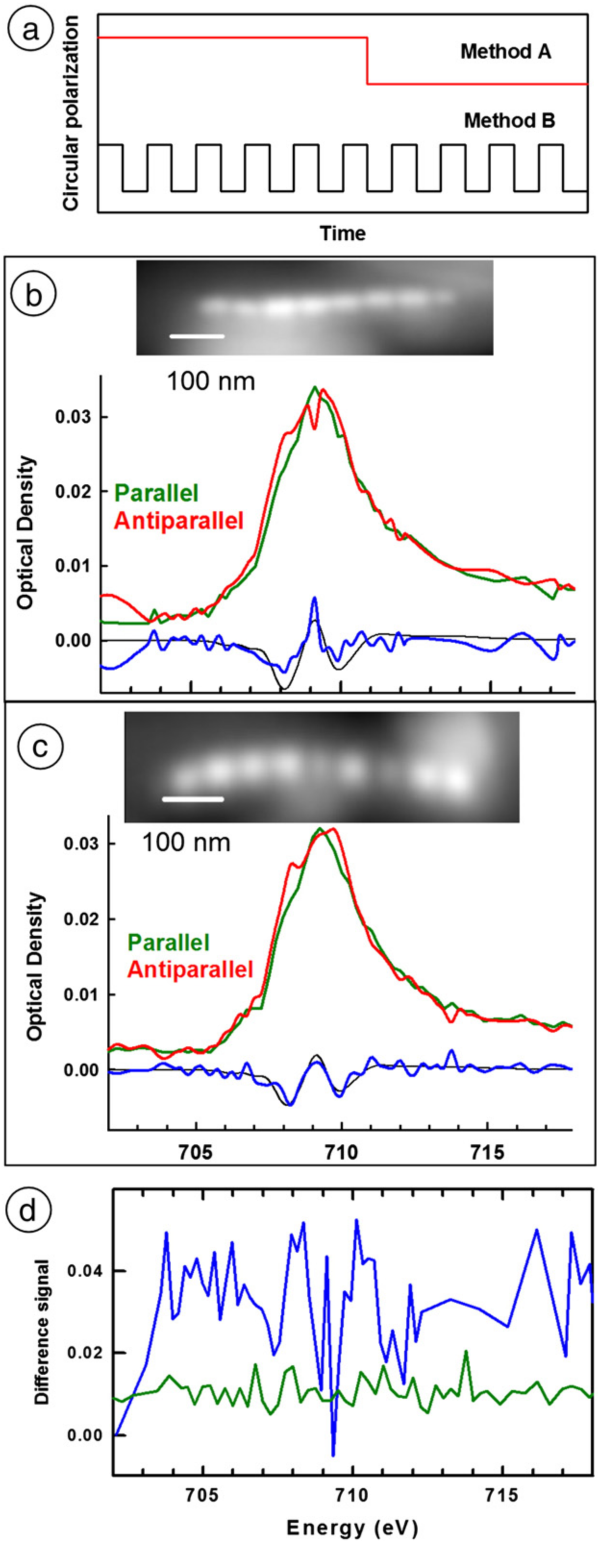

Fig. 1. (a) Schematic of two methods used to measure X-ray magnetic circular dichroism (XMCD). In method A (upper time plot) the left and right circular polarization data are acquired successively, with only a single switch of the circular polarization. In method B (lower time plot) — the left and right circular polarization data is obtained quasi concurrently by switching polarization at each photon energy. (b) Image, Fe 2p spectra and XMCD from a single magnetite magnetosome chain of a cell of *Candidatus* Magnetovibrio blakemorei strain MV-1 recorded with method A (successive mode). (c) Image, Fe 2p spectra and XMCD from a single MV-1 magnetosome chain recorded with method B (concurrent mode). In each case, the derived XMCD signal is plotted in comparison to that from mineral magnetite (black), (Goering et al., 2007) which has been scaled by 0.5. (d) Comparison of the noise in the data from the two measurements, derived in each case by subtracting the XMCD spectrum of mineral magnetite from that of the MV-1 magnetosome chain (blue: difference signal of method A; green: difference signal of method B).

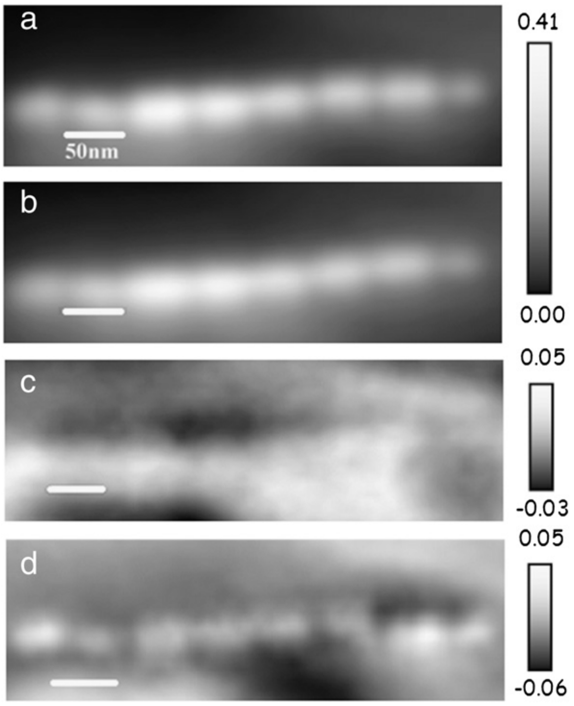

Fig. 2. Average of all images of an Fe L_3 XMCD image sequence measured with method A (successive mode) (a) Average of all images of the LCP stack; (b) Average of all images of the RCP stack; (c) The (LCP–RCP) difference in the pre-edge region (704–706 eV); (d) The (LCP–RCP) difference over the Fe L_3 peak (708–711 eV). Gray scales indicate the range of optical density (OD) or difference in optical density (ΔOD).

$OD_{709.8}$–OD_{704} images) is in red and the pre-Fe 2p signal at 704 eV (which is dominated by the cells and other non-Fe material), is in blue. The peak of the Fe L_3 signal occurs at 709.8 eV. However the OD at that energy also has contributions from the underlying absorption by the magnetite oxygen and non-Fe containing species. The latter signal is removed by subtracting the pre-Fe absorption image at 704 eV; thus, the ($OD_{709.8}$–OD_{704}) difference shows only the iron components. The single-domain magnetic iron particles in the chains synthesized by MTBs are found to have their magnetic vector pointing in the same direction in most cases. Assuming that the magnetic field (predominantly that of the earth) was present at the droplet when the sample was deposited and was uniform over the few tens of microns field of view of Fig. 5a, then one would expect the magnetic vector of each chain and thus, the cells, to be oriented along the magnetic field lines present at the droplet. However, Fig. 5a (and other lower magnification images sampling many more cells) shows that the cells of MV-1 are essentially randomly oriented. In contrast to the preferential orientation that probably occurs much of the time in their natural environment, MTB deposited on these TEM grids were not strongly oriented along the Earth's geomagnetic field. This is most likely due to turbulence in the droplet caused by the rapid capillary action that occurred when the excess fluid was wicked away. As the fluid is removed, the magnetic alignment of the cells is disturbed and the cells are unable to restore their natural ordering with the external magnetic field before they lose mobility due to the absence of liquid medium.

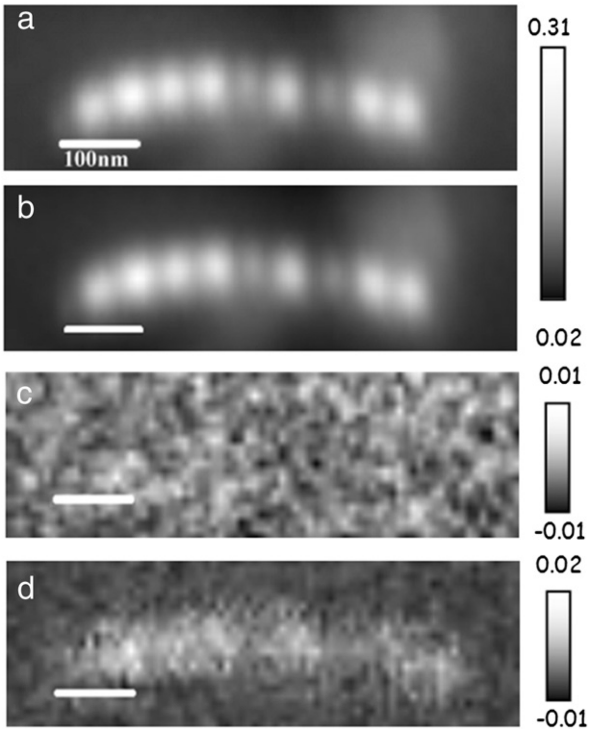

Fig. 3. Average of all images of a Fe L_3 XMCD image sequence measured with method B (concurrent mode). (a) The LCP stack; (b) Average of all images of the RCP stack; (c) The (LCP–RCP) difference in the pre-edge region (704–706 eV); (d) The (LCP–RCP) difference over of the Fe L_3 peak (708–711 eV). Gray scales indicate the OD or ΔOD range.

Fig. 6 presents results from a STXM-XMCD study of two overlapping MV-1 cells. An Fe L_3 image sequence was recorded using the concurrent XMCD polarization measurement mode. Fig. 6a displays the average of all images between 708.6 eV and 710 eV in the LCP mode which corresponds to the full Fe L_3 peak. The NEXAFS and XMCD spectra of the three colored regions (two individual magnetosomes and an overlap of two others) are presented in Fig. 6b–d. In each spectral plot the red curve is that recorded with RCP while the green curve is that recorded with LCP. For the green magnetosome (Fig. 6b), the LCP mode is the parallel spectrum while the RCP mode is the anti-parallel spectrum. The opposite is true for the red magnetosome (Fig. 6c) since the LCP mode has the anti-parallel and the RCP mode has the parallel spectral shape. Thus, the magnetic orientations of the two chains are opposite to one another. This is shown by the shapes of the RCP-LCP difference spectra (Fig. 6b, c) which are inverted relative to each other. The RCP-LCP difference spectrum of the horizontally-oriented MTB (red, Fig. 6c) shows the characteristic XMCD of magnetite while that of the more vertically-oriented MTB (green. Fig. 6c) shows the inverse of the magnetite XMCD reference spectrum. This example nicely illustrates that STXM-XMCD is sensitive to both the magnitude and orientation of the magnetic vector of individual magnetosomes. This is further exemplified by the signal extracted from the intersection of the two chains (Fig. 6d), where the XMCD signal disappears due to the additive nature and opposite orientation of the XMCD from the two magnetosomes in this region.

Fig. 7a compares the corrected average XMCD spectrum from both chains (inset of Fig. 7a indicates the regions of the specific magnetosomes from each chain that were selected for measurements), in comparison to the XMCD spectrum of mineral magnetite. Selecting just the central part of the best aligned magnetosomes gives the best possible representation of the magnetic signal since the signal from the edges of the magnetosomes is relatively reduced due to the finite spatial resolution of STXM and the wings of the response function (Leontowich et al., 2011). The Fe L_3 component for each chain was isolated and matched to the edge-jump normalized data reported by Goering et al. (2007), as described in experimental Section 2.3. The tilted chain (red in Fig. 7a) has a reduced magnetic moment (only the projection on the horizontal axis is sensed) and its orientation is opposite to that of the horizontal chain (green in Fig. 7a). Prior to averaging with the XMCD of the two chains, the XMCD from the tilted chain was inverted and then rescaled by a factor of −1.30 to account for the 40° in-plane tilt from horizontal. As shown in Fig. 7a, the match on an absolute scale of the corrected, averaged XMCD from these two chains to the XMCD of abiotic

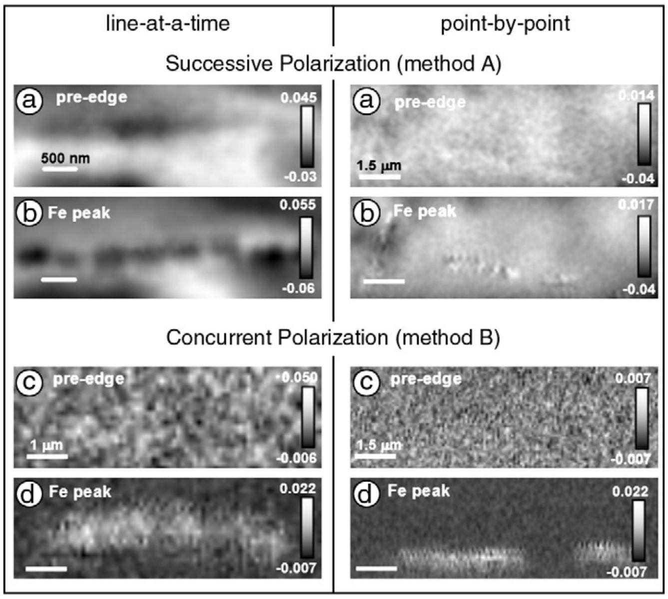

Fig. 4. Comparison of Fe L_3 XMCD data recorded using (left) line-at-a-time mode; and (right) point-by-point scanning for successive (upper block of 4 images) and concurrent (lower block of 4 images) modes. Within each block, the upper figures (labeled a or c) are the differences averaged over a region of pre-edge energies (704.5 to 706.5 eV) for opposite circular polarization (LCP–RCP), while the lower images (labeled b or d) are the differences integrated over the Fe L_3 peak energies (707.5 to 711.5 eV) for opposite circular polarization (LCP–RCP). The concurrent mode shows less statistical variation as well as less absolute variation in the optical density between the two polarization images. Gray scales indicate the ΔOD range.

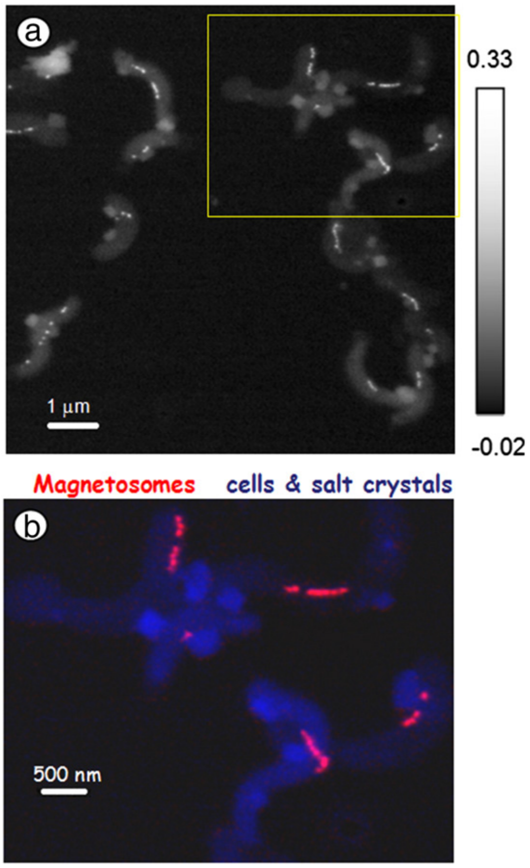

Fig. 5. (a) STXM OD image at 709.8 eV of a number of cells of strain MV-1; (b) a false color image of the upper right area in Fig. 6a, where the iron signal (from $OD_{709.8}$–OD_{704}) is in red and the pre-Fe 2p signal at 704 eV is in blue.

magnetite is excellent. Integration of the absolute value of that XMCD from the MV-1 magnetosome magnetite compared to that from abiotic magnetite gives a ratio of 0.93(6) for the magnetic signal of MV-1 magnetosomes relative to that of magnetite. Since the magnetic moment of magnetite is 3.9 μB (Goering et al., 2006a, 2006b, 2007), our result for this set of two MV-1 chains is an average moment of 3.6(2) μB.

An approach to look for possible anomalies in the magnetosome XMCD signal, perhaps associated with partial site occupancy (Coker et al., 2007), is to create "XMCD images" from each peak of the L_3 signal, which are more or less specific to each of the 3 crystal sites. Fig. 7b–d are images of the XMCD signal averaged over each of the three characteristic peaks of the XMCD. Except for the cross-over point where the overlap of opposite oriented signals nearly cancels the XMCD signal (see Fig. 6d), there is a clear signal in each channel, with approximately similar signal levels, taking into account the very small amount of magnetic material contributing to the signal. In each channel, the sense of the XMCD signal is opposite between the two magnetosomal chains and is inverted for Fig. 7c relative to Fig. 7b and 7d, which is consistent with the extracted XMCD spectra.

3.3. Biochemical mapping of cells of strain MV-1

C 1s and O 1s image sequences were measured from several cells of strain MV-1 in order to map the biochemical components of the cells. Fig. 8a presents the reference spectra for protein (albumin, green), polysaccharide (modeled as glucose, red) and $CaCO_3$ (blue) reported by Lawrence et al. (2003), which were used to generate component maps from a C 1s image sequence using singular value decomposition (SVD) (Ade and Hitchcock, 2008). SVD is a matrix decomposition method used to rapidly find the optimum solution to a set of linear equations which are highly over-determined. The output of the SVD analysis is a set of maps for each component for which a reference spectrum is provided. Fig. 8b is a false-color image of the spatial distributions of protein (red), polysaccharide (green) and $CaCO_3$ (blue). A principal component analysis (PCA) and a subsequent cluster analysis (Lerotic et al., 2005; Jacobsen, 2011) were also performed. This multivariate statistical analysis technique first transforms the data into a set of ranked, orthogonalized variables (or principal components) and then seeks clustering in the principal component variable space which identifies spectrally unique components. PCA combined with cluster and target analysis provides unsupervised mapping of spectrally distinct regions as well as extraction of their spectra. PCA/cluster analysis of the C 1s image sequence identified three spatial regions that have distinct absorption spectra (Fig. 8c) which were identified by this approach as the interior cellular structure (green), the extracellular polymeric substance (EPS) (red) and a mineral region (blue). The spectra of the cellular region and the EPS are similar, with the largest difference being a higher optical density inside the cell which gives clear definition to the MV-1 cells. Also, in the EPS region there is an increase, relative to the characteristic protein spectral features at 285.15 eV and 288.20 eV, in the height of the polysaccharide NEXAFS peak at 289.35 eV. The differentiation of the cell and EPS was further confirmed by the SVD analysis (Fig. 8b). The spectrum of the third region (mineral, blue) has less well defined C 1s spectral structure and a much larger non-carbon signal. This is consistent with its attribution to a mineral material, as is also supported by the close match in location to the region of high $CaCO_3^{2-}$ concentration found by the SVD analysis (Fig. 8b). The peaks at 297 and 300 eV in the cellular (green) and EPS (red) spectra (Fig. 8c) are from potassium ions.

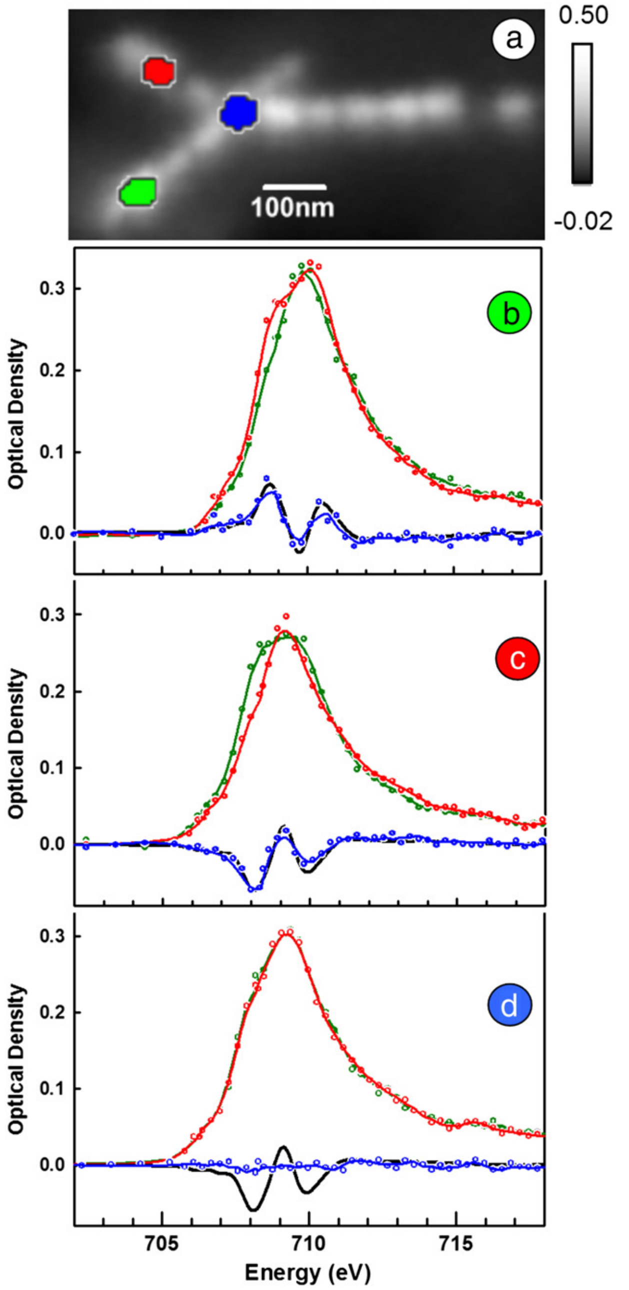

Fig. 6. (a) Average of images in the Fe L_3 peak (708.6–710 eV) of the magnetosome chains of two overlapping MV-1 cells. (b) to (d) present the Fe L_3 LCP/RCP spectra of the three colored areas shown in (a), along with their difference spectra (RCP-LCP) . In each case, the red spectrum is that recorded with RCP while the green spectrum is that recorded with LCP; (b) data for the green magnetosome; (c) data for the red magnetosome; (d) data for the blue magnetosome. Black lines in Fig. 6(b)–(d) are scaled XMCD spectra of reference magnetite (Goering et al., 2007). (For interpretation of the references to color in this figure legend, the reader is referred to the web version of this article.)

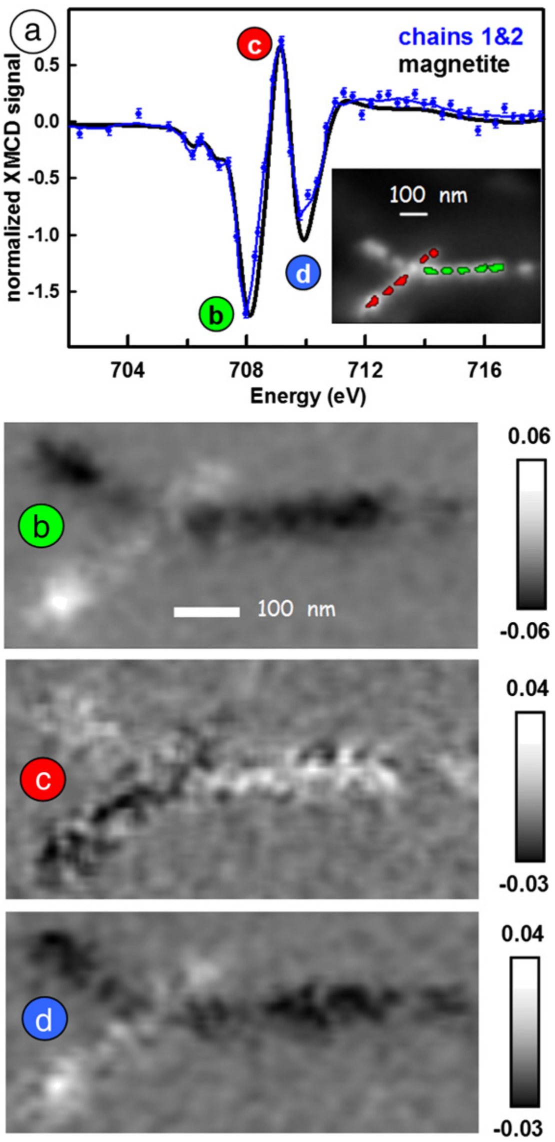

Fig. 7. (a) Corrected average XMCD spectra of the two chains (data points: blue dots with error bars; blue line, smoothed guide to the eye; inset image with red and green markers indicates the areas from which spectral data was extracted) compared to that of mineral magnetite (black, Goering et al., 2007). The RCP and LCP spectra of each chain were background subtracted and the intensity scaled to match the edge-normalized data of Goering et al. (2007). See text for description of how the two opposing polarity signals were scaled and averaged. The XMCD data of mineral magnetite was reduced by 50% to account for the 30° azimuthal tilt angle of the MV-1 sample. (b) Image of the XMCD signal that is a composite of images from 707.8–708.5 eV corresponding to the first, negative peak in the XMCD spectrum shown in 7a; (c) Image of the XMCD signal that is a composite of images from 709 to 709.3 eV corresponding to the second, positive peak in the XMCD spectrum shown in 7a; (d) Image of the XMCD signal that is a composite of images from 709.9 to 710.5 eV corresponding to the third, negative peak in the XMCD spectrum shown in 7a. (For interpretation of the references to color in this figure legend, the reader is referred to the web version of this article.)

The O 1s analysis is more complex, because the O 1s edge has contributions from both the magnetosome and organic components of bacteria. Fig. 9a shows the average of all images from 524.0 to 560.8 eV. In addition to the MV-1 cells, salt crystals and magnetosome chains are clearly visible. The spectra of these regions are shown in Fig. 9b along with O 1s reference spectra of magnetite and protein. The O 1s spectrum of the magnetosomes (red curve in Fig. 9b) was generated by subtracting the O 1s spectrum of the adjacent cellular material from the spectrum extracted at the location of the magnetosomes. The amount of cellular signal subtracted is such that there is almost equal O 1s contribution from the organic material and magnetite. After this processing, there is a good match between the O 1s spectra of the magnetosomes and magnetite (red and black curves in Fig. 9b). The cellular component (green in Fig. 9b) shows a close match to that of reference albumin at the main O 1s → $\pi^*_{C=O}$ peak (532.1 eV). However, the $\sigma^*_{C\text{–}O}$ signal in the continuum region (536–546 eV) is much larger in the cellular spectrum than in the spectrum of pure protein, due to the presence of many other

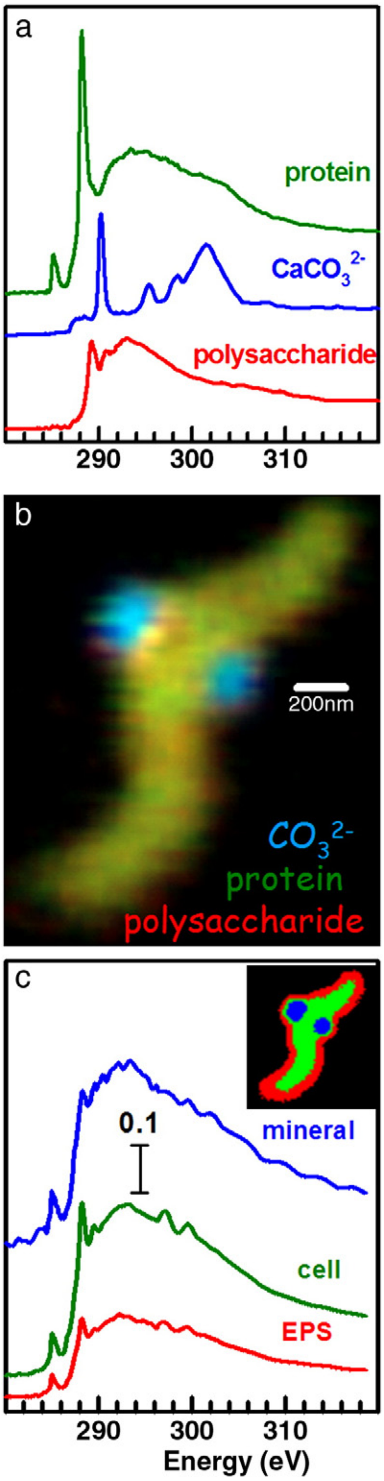

Fig. 8. (a) C 1s reference spectra of protein (human serum albumin, green), $CaCO_3$ (calcite, blue) and polysaccharide (represented as glucose, red) (Lawrence et al., 2003). (b) Color-coded composite of the 3 component maps derived by fitting the reference spectra of Fig. 8a to a C 1s image sequence from an MV-1 magnetotactic bacterial cell (same color-coding as in Fig. 8a). (c) The spectra of the spatial regions indicated in the inset RGB composite, which were identified by a combination of principle component and cluster analysis. The peaks at 297 eV and 300 eV arise from K^+. See text for further details.

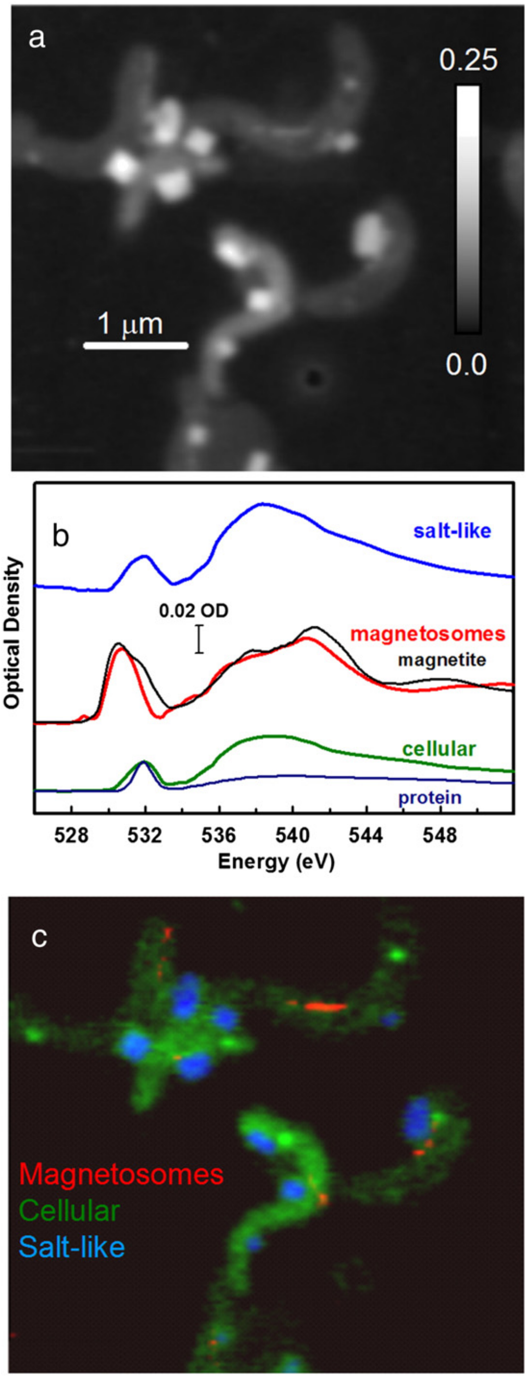

Fig. 9. (a) Average of all images of an O 1s stack (524.0–560.8 eV). (b) Spectra extracted from the cellular regions, the magnetosome chain, and the salt crystals. The displayed spectrum of the magnetosome chain has had the signal from the surrounding cellular material subtracted. The O 1s spectra of magnetite (black) and protein (dark blue) are plotted for comparison. (c) Color-coded composite of magnetosome (red), cellular (green) and salt-like (blue) component maps derived by fitting the reference spectra of Fig. 9b to the O 1s image sequence (see text for further details).

oxygen containing species, such as lipids and polysaccharides, within the body of the MTB cell. Lipids and polysaccharides have little or no signal around 532 eV but much larger signal than protein in the 536–544 eV region due to their aliphatic character which leads to strong O 1s → $\sigma^*_{C\text{–}O}$ transitions. Detection of the magnetite magnetosomes at the O 1s edge is more difficult than at the Fe 2p edge because the magnetite-specific O 1s feature is relatively weak. However, it is possible to map the magnetosomes because magnetite has a low-lying O 1s → (O 2p – Fe 3 d) peak at 530.2 eV, which is at a lower energy than the lowest energy biological signal, the O 1s → $\pi^*_{C=O}$ peak of protein at 532.1 eV. The O 1s NEXAFS spectra of protein, pure mineral magnetite and the mineral inclusions were used to fit the O 1s stack and thus visualize magnetosomes from their O 1s signal. Fig. 9c is a color-coded composite of the magnetosome (red), cellular (green) and salt (blue) components determined by an SVD analysis of the O 1s image sequence.

4. Discussion

The use of concurrent polarization mode (method B) (Figs. 1–3) and point-by-point image acquisition (Fig. 4) for STXM-XMCD has resulted in significantly improved results relative to our previously reported spatial resolved XMCD measurements (Lam et al., 2010). The current study demonstrates improvement of XMCD spectra obtained from individual magnetosomes as well as from full chains. Lam et al. (2010) suggested that there was a difference between the Fe (II)/Fe (III) ratio of the MV-1 MTB magnetite and that of abiotic mineral magnetite. However, this more accurate study finds a much smaller difference between the XMCD of magnetosome magnetite and that of abiotic magnetite. The previously observed higher relative amount of Fe (II) may have been an artifact of radiation damage, which reduces Fe (III) to Fe (II), as reported by Toner et al. (2005) and Yano et al. (2005). The improved efficiency of the polarization-switching mode has significantly reduced the impact of radiation damage on STXM-XMCD measurements. Radiation damage in STXM has two effects: contamination of the sample surface (mainly with build-up of carbonaceous material) and photoreduction. By changing our measurement method, the optical density distortions due to radiation-induced carbon build-up are minimized and the total dose used is reduced so there is less photoreduction of the magnetite.

The quantitative XMCD signal averaged over the two chains of magnetite magnetosomes (Fig. 7a) is in nearly quantitative agreement with the XMCD of mineral magnetite (Goering et al., 2007). There still appears to be a slightly higher Fe (II)/Fe (III) ratio in the biological magnetite relative to mineral magnetite, but the effect is much less pronounced than reported by Lam et al. (2010). In addition, although a weak effect, the Fe (II) XMCD peak appears to be shifted to slightly lower energy relative to its counterpart in the XMCD spectrum of mineral magnetite (Goering et al., 2007) and there are other minor differences in the region of the XMCD signal from the Fe (III) O_h site (see Fig. 7a). We have shown it is possible to visualize magnetosomes at the O 1s edge (see Fig. 9) despite the much larger O 1s signal from biological material. This is the first time that magnetosome chains have been mapped using O 1s spectromicroscopy.

This study is a good example of how NEXAFS and XMCD signals recorded at high spatial resolution in STXM provide a highly sensitive probe of both the biochemistry and the magnetization. The ability to measure both the magnitude and the direction of the magnetization has great potential to provide additional insight into magnetosome biomineralization mechanisms. XMCD, along with NEXAFS, may yield important information regarding the fate of magnetosomes during cell division, such as elucidating how magnetosome chains split and grow within daughter cells. Previous studies have relied on TEM to investigate the distribution of magnetosomes during cell division (Staniland et al., 2010). We are striving to use gentler sample preparation methods to allow for passive alignment of bacteria — for example, introduction of X-ray transparent Si_3N_4 windows into culture, as outlined by Lawrence et al. (2003). STXM-XMCD studies of such samples may yield further information on the biochemical or environmental mechanisms that lead to “south-seeking” behavior (in the northern hemisphere), which is observed in a minority of cells in all cultures of polar magnetotactic bacteria, including MV-1. Note that a south-seeking cell adjacent to a north seeking cell is one possible explanation of the opposite polarity of moments found in the set of MV-1 cells presented in Figs. 6, and 7. Another aspect of magnetotactic bacteria that could be studied effectively with STXM-XMCD is the nature and effect of gaps between chains of magnetosomes exhibited within a single cell by some magnetotactic species grown in culture. Examples of these gaps are clearly visible in Figs. 5 and 6a. Bazylinski et al. (1995) commented on the presence of these gaps in cells of strain MV-1 and suggested that, since all the elongated crystals were aligned along their long axes within the cell, the different parts of the magnetosome chain would also be magnetized in the same direction. Since electron holographic studies map field lines rather than explicitly measure the magnetization of individual magnetosomes it might be difficult to verify that point with electron holography. Thus, the ability of STXM-XMCD to study the orientation and magnitude of the magnetism of each magnetosome within a cell could add significantly to other methods being used to investigate this fascinating biomineralization system.

Acknowledgments

This work was supported by NSERC (Canada) (Hitchcock) and by the U.S. National Science Foundation grant EAR-0920718 (Bazylinski). We thank Dr. Eberhard Goering (MPI-Metallforschung, Stuttgart) for supplying the Fe L_{23} and XMCD reference spectra of magnetite. We thank two anonymous referees for useful suggestions for improvements to the initial manuscript. The XMCD studies were carried out at the STXM on beamline 10ID1 at the Canadian Light Source (CLS), which is supported by the Canada Foundation for Innovation (CFI), NSERC, Canadian Institutes of Health Research (CIHR), National Research Council (NRC) and the University of Saskatchewan. We thank Drs. Jian Wang and Chithra Karunakaran for their expert support at the CLS. The C 1s and O 1s data was measured at the STXM on beamline 11.0.2 at the Advanced Light Source (ALS), which is supported by the Director, Office of Energy Research, Office of Basic Energy Sciences, Materials Sciences Division of the U.S. Department of Energy, under Contract no. DE-AC02-05CH11231. We thank Dr. Tolek Tyliszczak for his expert support of the ALS instrumentation.

References

Ade, H., Hitchcock, A.P., 2008. NEXAFS microscopy and resonant scattering: composition and orientation probed in real and reciprocal space. Polymer 49, 643–675.

Albrecht, M., Janke, V., Sievers, S., Siegner, U., Schüler, D., Heyen, U., 2005. Scanning force microscopy study of biogenic nanoparticles for medical applications. Journal of Magnetism and Magnetic Materials 290–291, 269–271.

Antonov, V.N., Harmon, B.N., Yaresko, A.N., 2003. Electronic structure and x-ray magnetic circular dichroism in Fe_3O_4 and Mn-, Co-or Ni-substituted Fe_3O_4. Physical Review B 67, 024417.

Bazylinski, D.A., 1995. Structure and function of the bacterial magnetosome. ASM News 61, 337–343.

Bazylinski, D.A., Frankel, R.B., 2004. Magnetosome formation in prokaryotes. Nature Reviews Microbiology 2, 217–230.

Bazylinski, D.A., Frankel, R.B., Heywood, B.R., Mann, S., King, J.W., Donaghay, P.L., Hanson, A.K., 1995. Controlled biomineralization of magnetite (Fe_3O_4) and greigite (Fe_3S_4) in a magnetotactic bacterium. Applied and Environmental Microbiology 61, 3232–3239.

Bellini, S., 1963a. Su di un particolare comportamento di batteri d'acqua dolce (On a unique behavior of freshwater bacteria). Institute of Microbiology, University of Pavia, Italy. internal report.

Bellini, S., 1963b. Ulteriori studi sui “batteri magnetosensibili” (Further studies on magnetosensitive bacteria). Institute of Microbiology, University of Pavia, Italy. internal report.

Bellini, S., 2009. Further studies on “magnetosensitive bacteria”. Chinese Journal of Oceanology and Limnology 27, 6–12.

Blakemore, R.P., 1975. Magnetotactic bacteria. Science 190, 377–379.

Carvallo, C., Sainctavit, P., Arrio, M., Menguy, N., Wang, Y., Ona-Nguema, G., Brice-Profeta, S., 2008. Biogenic vs. abiogenic magnetite nanoparticles: a XMCD study. American Mineralogist 93, 880–885.

Ceyhan, B., Alhorn, P., Lang, C., Schüler, D., Niemeyer, C.M., 2006. Semisynthetic biogenic magnetosome nanoparticles for the detection of proteins and nucleic acids. Small 2, 1251–1255.

Charilaou, M., Winklhofer, M., Gehring, A.U., 2011. Simulation of ferromagnetic resonance spectra of linear chains of magnetite nanocrystals. Journal of Applied Physics 109, 093903.

Coker, V.S., Pattrick, R.A.D., van der Laan, G., Lloyd, J.R., 2006. Formation of Magnetic Minerals by Non-Magnetotactic Prokaryotes in Magnetoreception and Magnetosomes in Bacteria. : Microbiol Monograph, 3. Springer, Heidelberg, pp. 275–301.

Coker, V.S., Pearce, C.I., Lang, C., van der Laan, G., Pattrick, R.A.D., Telling, N.D., Schüler, D., Arenholz, E., Lloyd, J.R., 2007. Cation site occupancy of biogenic magnetite compared to polygenic ferrite spinels determined by X-ray magnetic circular dichroism. European Journal of Mineralogy 19, 707–716.

Coker, V.S., Pearce, C.I., Pattrick, R.A.D., van der Laan, G., Charnock, J.M., Telling, N.D., Arenholz, E., Lloyd, J.R., 2008. Probing the site occupancies of Co-, Ni-, and Mnsubstituted biogenic magnetite using XAS and XMCD. American Mineralogist 93, 1119–1132.

Coker, V.S., Telling, N.D., van der Laan, G., Pattrick, R.A.D., Pearce, C.I., Arenholz, E., Tuna, F., Winpenny, R.E.P., Lloyd, J.R., 2009. Harnessing the extracellular bacterial production of nanoscale cobalt ferrite with exploitable magnetic properties. ACS Nano 3, 1922–1925.

Coker, V.S., Byrne, J.M., Telling, N.D., van der Laan, G., Lloyd, J.R., Hitchcock, A.P., Wang, J., Pattrick, R.A.D., in press. The application of STXM-XMCD to characterise the bio-geo interface during the dissimilatory reduction of Fe (III)-oxyhydroxide, Geobiology.

Dean, A.J., Bazylinski, D.A., 1999. Genome analysis of several magnetotactic bacterial strains using pulsed-field gel electrophoresis. Current Microbiology 39, 219–225.

Dunin-Borkowski, R.E., McCartney, M.R., Frankel, R.B., Bazylinski, D.A., Pósfai, M., Buseck, P.R., 1998. Magnetic microstructure of magnetotactic bacteria by electron holography. Science 282, 1868–1870.

Dunlop, D.J., 1973. Superparamagnetic and single-domain threshold sizes in magnetite. Journal of Geophysical Research Solid Earth 78, 1780–1793.

Egli, R., 2004. Characterization of individual rock magnetic components by analysis of remanance curves. 1. Unmixing natural sediments. Studia Geophysica et Geodaetica 48, 391–446.

Fischer, H., Mastrogiacomo, G., Löffler, J.F., Warthmann, R.J., Weidler, P.G., Gehring, A.U., 2008. Ferromagnetic resonance and magnetic characteristics of intact magnetosome chains in Magnetospirillum gryphiswaldense. Earth and Planetary Science Letters 270, 200–208.

Frankel, R.B., Bazylinski, D.A., 1994. Magnetotaxis and magnetic particles in bacteria. Hyperfine Interactions 90, 135–142.

Frankel, R.B., Blakemore, R.P., 1980. Navigational compass in magnetic bacteria. Journal of Magnetism and Magnetic Materials 15–18, 1562–1564.

Frankel, R.B., Blakemore, R.P., Wolfe, R.S., 1979. Magnetite in freshwater magnetic bacteria. Science 203, 1355–1357.

Goering, E., Justen, M., Geissler, J., Rüdiger, U., Rabe, M., Untherodt, G.G., Schütz, G., 2002. Magnetic anisotropy of textured CrO_2 thin films investigated by X-ray magnetic circular dichroism. Applied Physics A: Materials Science & Processing 75, 747–753.

Goering, E., Gold, S., Lafkioti, M., Schütz, G., 2006a. Vanishing Fe 3d orbital moments in single-crystalline magnetite. Europhysics Letters 73, 97–103.

Goering, E., Lafkioti, M., Gold, S., 2006b. Comment on "Spin and Orbital Magnetic Moments of Fe3O4". Physical Review Letters 96, 039701.

Goering, E.J., Lafkioti, M., Gold, S., Scheutz, G., 2007. Absorption spectroscopy and XMCD at the Verwey transition of Fe_3O_4. Journal of Magnetism and Magnetic Materials 310, e249–e251.

Gorby, Y.A., Beveridge, T.J., Blakemore, R.P., 1988. Characterization of the bacterial magnetosome membrane. Journal of Bacteriology 170, 834–841.

Heywood, B.R., Bazylinski, D.A., Garratt-Reed, A.J., Mann, S., Frankel, R.B., 1991. Controlled biosynthesis of greigite (Fe_3S_4) in magnetotactic bacteria. Naturwissenschaften 77, 536–538.

Howells, M., Jacobsen, C., Warwick, T., 2007. In: Hawkes, P.W., Spence, J.C.H. (Eds.), Principles And Applications of Zone Plate X-Ray Microscopes in Science of Microscopy. Springer, NY.

Huang, D.J., Chang, C.F., Jeng, H.-T., Guo, G.Y., Lin, H.-J., Wu, W.B., Ku, H.C., Fujimori, A., Takahashi, Y., Chen, C.T., 2004. Spin and orbital magnetic moments of Fe_3O_4. Physical Review Letters 93 (077204), 1–4.

Jacobsen, C.J.J., 2011. PCA_GUI and other useful IDL routines for analysis of soft X-ray microscopy data is available at http://xrm.phys.northwestern.edu (last accessed, 24-Feb-2011).

Jimenez-Lopez, C., Romanek, C.S., Bazylinski, D.A., 2010. Magnetite as a prokaryotic biomarker: a review. Journal of Geophysical Research Biogeosciences 115, G00G03.

Johansson, G.A., Tyliszczak, T., Mitchell, G.E., Keefe, M., Hitchcock, A.P., 2007. Three dimensional chemical mapping by scanning transmission X-ray spectromicroscopy. Journal of Synchrotron Radiation 14, 395–402.

Kaznatcheev, K.V., Karunakaran, C., Lanke, U.D., Urquhart, S.G., Obst, M., Hitchcock, A.P., 2007. Soft X-ray spectromicroscopy beamline at the CLS: commissioning results. Nuclear Instruments and Methods in Physics Research Section A 582, 96–99.

Kilcoyne, A.L.D., Tylisczak, T., Steele, W.F., Fakra, S., Hitchcock, P., Franck, K., Anderson, E., Harteneck, B., Rightor, E.G., Mitchell, G.E., Hitchcock, A.P., Yang, L., Warwick, T., Ade, H., 2003. Interferometrically controlled scanning transmission microscopes at the advanced light source. Journal of Synchrotron Radiation 10, 125–136.

Komeili, A., Hojatollah, V., Beveridge, T.J., Newmann, D.K., 2004. Magnetosome vesicles are present before magnetite formation, and MamA is required for their activation. Proceedings of the National Academy of Sciences of the United States of America 101, 3839–3844.

Kuiper, P., Searle, B.G., Duda, L.-C., Wolf, R.M., van der Zaag, P.J., 1997. Fe $L_{2,3}$ linear and circular dichroism of Fe_3O_4. Journal of Electron Spectroscopy and Related Phenomena 86, 107–113.

Lam, K.P., Hitchcock, A.P., Obst, M., Lawrence, J.R., Swerhone, G.D.W., Leppard, G.G., Tyliszczak, T., Karunakaran, C., Wang, J., Kaznatcheev, K., Bazylinski, D.A., Lins, U., 2010. X-ray magnetic circular dichroism of individual magnetosomes by Scanning Transmission X-ray Microscopy. Chemical Geology 270, 110–116.

Lawrence, J.R., Swerhone, G.D.W., Leppard, G.G., Araki, T., Zhang, X., West, M.M., Hitchcock, A.P., 2003. Scanning transmission X-ray, laser scanning, and transmission electron microscopy mapping of the exopolymeric matrix of microbial biofilms. Applied and Environmental Microbiology 69, 5543–5554.

Leonov, I., Yaresko, A.N., Antonov, V.N., Korotin, M.A., Anisimov, V.I., 2004. Charge and orbital order in Fe_3O_4. Physical Review Letters 93, 146404.

Leonov, I., Yaresko, A.N., Antonov, V.N., Anisimov, V.I., 2006. Electronic structure of charge-ordered Fe_3O_4 from calculated optical, magneto-optical Kerr effect, and O K-edge x-ray absorption spectra. Physical Review B 74, 165117.

Leontowich, A.F.G., Tyliszczak, T., Hitchcock, A.P., 2011. Measurement of the point spread function of a soft X-ray microscope by single pixel exposure of photoresists. In: Juha, L. (Ed.), Damage to VUV, EUV, and X-ray Optics: Proc. SPIE, 8077, pp. 0–8.

Lerotic, M., Jacobsen, C., Gillow, J.B., Francis, A.J., Wirick, S., Vogt, S., Maser, J., 2005. Cluster analysis in soft X-ray spectromicroscopy: finding the patterns in complex specimens. Journal of Electron Spectroscopy and Related Phenomena 144–147, 1137–1143.

Martel, S., Mohammadi, M., Felfoul, O., Lu, Z., Pouponneau, P., 2009. Flagellated magnetotactic bacteria as controlled MRI-trackable propulsion and steering systems for medical nanorobots operating in the human microvasculature. International Journal of Robotics Research 28, 571–582.

McCartney, M.R., Lins, U., Farina, M., Buseck, P.R., Frankel, R.B., 2001. Magnetic microstructure of bacterial magnetite by electron holography. European Journal of Mineralogy 13, 685–689.

Moskowitz, B.M., Frankel, R.B., Bazylinski, D.A., 1993. Rock magnetic criteria for the detection of biogenic magnetite. Earth and Planetary Science Letters 120, 283–300.

Najafi, E., Hernández Cruz, D., Obst, M., Hitchcock, A.P., Douhard, B., Pireaux, J.-J., Felten, A., 2008. Polarization dependence of the C 1s X-ray absorption spectra of individual multi-walled carbon nanotubes. Small 4, 2279–2285.

Nolle, D., Goering, E., Tietze, T., Schütz, G., Figuerola, A., Manna, L., 2009. Structural and magnetic deconvolution of FePt/FeOx-nanoparticles using x-ray magnetic circular dichroism. New Journal of Physics 11, 033034.

Pattrick, R.A.D., van der Laan, G., Henderson, C.M.B., Kuiper, P., Dudzik, E., Vaughan, D.J., 2002. Cation site occupancy in spinel ferrites studied by X-ray magnetic circular dichroism: developing a method for mineralogists. European Journal of Mineralogy 14, 1095–1102.

Pellegrin, E., Hagelstein, M., Doyle, S., Moser, H.O., Fuchs, J., Vollath, D., Schuppler, S., James, M.A., Saxena, S.S., Niesen, L., Rogojanu, O., Sawatzky, G.A., Ferrero, C., Borowski, M., Tjernberg, O., Brookes, N.B., 1999. Characterization of nanocrystalline g-Fe_2O_3 with synchrotron radiation techniques. Physica Status Solidi B 215, 797.

Pérez, N., Bartolomé, F., García, L.M., Bartolomé, J., Morales, M.P., Serna, C.J., Labarta, A., Batlle, X., 2009. Nanostructural origin of the spin and orbital contribution to the magnetic moment in Fe3–xO4 magnetite nanoparticles. Applied Physics Letters 94 (093108), 1–3.

Simpson, E.T., Kasama, T., Posfai, M., Buseck, P.R., Harrison, R.J., Dunin-Borkowski, R.E., 2005. Magnetic induction mapping of magnetite chains in magnetotactic bacteria at room temperature and close to the Verwey transition using electron holography. Journal of Physics Conference Series 17, 108–121.

Staniland, S., Ward, B., Harrison, A., van der Laan, G., Telling, N., 2007. Rapid magnetosome formation shown by real-time x-ray magnetic circular dichroism. Proceedings of the National Academy of Sciences of the United States of America 104, 19524–19528.

Staniland, S., Williams, W., Telling, N., van der Laan, G., Harrison, A., Ward, B., 2008. Controlled cobalt doping of magnetosomes in vivo. Nature Nanotechnology 3, 158–162.

Staniland, S.S., Moisescu, C., Benning, L.G., 2010. Cell division in magnetotactic bacteria splits magnetosome chain in half. Journal of Basic Microbiology 50, 392–396.

Stöhr, J., 1991. NEXAFS spectroscopy. Springer Tracts in Surface Science, 25. Springer, Berlin.

Stöhr, J., 1999. Exploring the microscopic origin of magnetic anisotropies with X-ray Magnetic Circular Dichroism (XMCD) spectroscopy. Journal of Magnetism and Magnetic Materials 200, 470–497.

Stöhr, J., Siegmann, H.C., 2006. Magnetism: From Fundamentals to Nanoscale Dynamics, Springer Series in Solid-State Sciences. Springer, Berlin.

Thomas-Keprta, K.L., Bazylinski, D.A., Kirschvink, J.L., Clemett, S.J., McKay, D.S., Wentworth, S.J., Vali, H., Gibson Jr., E.K., Romanek, C.S., 2000. Elongated prismatic magnetite crystals in ALH84001 carbonate globules: potential Martian magnetofossils. Geochimica et Cosmochimica Acta 64, 4049–4081.

Toner, B., Fakra, S., Villabos, N., Warwick, T., Sposito, G., 2005. Spatially resolved characterization of biogenic manganese oxide production within a bacterial biofilm. Applied and Environmental Microbiology 71, 1300–1310.

Weiss, B.P., Kim, S.S., Kirschvink, J.L., Kopp, R.E., Sankaran, M., Kobayashi, A., Komeili, A., 2004. Ferromagnetic resonance and low-temperature magnetic tests for biogenic magnetite. Earth and Planetary Science Letters 224, 73–89.

Yano, J., Kern, J., Irrgang, K.D., Latimer, M.J., Bergmann, U., Glatzel, P., Pushkar, P., Biesiadka, J., Loll, B., Sauer, K., Messinger, J., Zouni, A., Yachandra, V.K., 2005. X-ray damage to the Mn_4Ca complex in single crystals of photosystem II: A case study for metalloprotein crystallography. Proceedings of the National Academy of Sciences of the United States of America 102, 12047–12052.